3D osteocyte lacunar morphometry of human bone biopsies with high resolution microCT: from monoclonal gammopathy to newly diagnosed multiple myeloma

Inés Moreno-Jiménez[1*], Sharen Heinig[1], Unai Heras[2], Daniela Simone Maichl[3], Susanne Strifler[3], Ellen Leich-Zbat[3,4], Stéphane Blouin[5], Peter Fratzl[1], Nadja Fratzl-Zelman[5], Franziska Jundt[3,6*], Amaia Cipitria[1,2,7*]

[1] Max Planck Institute of Colloids and Interfaces, Department of Biomaterials, 14476 Potsdam, Germany

[2] Group of Bioengineering in Regeneration and Cancer, Biodonostia Health Research Institute, 20014 San Sebastian, Spain.

[3] Department of Internal Medicine II, University Hospital Würzburg, 97080 Würzburg, Germany

[4] Institute of Pathology, University of Würzburg, 97080 Würzburg, Germany

[5] Ludwig Boltzmann Institute of Osteology at the Hanusch Hospital of OEGK and AUVA Trauma Centre Meidling, Vienna, Austria.

[6] Comprehensive Cancer Center Mainfranken, 97080 Würzburg, Germany

[7] IKERBASQUE, Basque Foundation for Science, 48009 Bilbao, Spain.

[(*)] Correspondence to: ines.moreno@mpikg.mpg.de; Jundt_f@ukw.de; amaia.cipitria@mpikg.mpg.de; amaia.cipitria@biodonostia.org

Abstract

Osteocytes are bone-embedded cells connected via canaliculi and they regulate the bone resorption/formation balance. Osteocyte function is altered in skeletal disorders including cancer. Multiple myeloma (MM) is a hematological malignancy, whereby plasma cells disrupt the bone homeostasis and induce excessive resorption of the mineralized extracellular matrix (ECM), as evidenced by clinical computed tomography (CT). However, morphometric analyses of the mineralized ECM and bone microporosity are not yet performed in patients with MM, nor in the precursor conditions of monoclonal gammopathy of undetermined significance (MGUS) and smoldering MM (SMM). Here, we characterize changes in 3D osteocyte lacunar morphology in bone biopsy samples obtained from patients with MGUS, SMM and newly diagnosed MM, using high resolution microCT. In the small lacunae 20-900 μm^3 range, we found a trend for lower lacunar density and increasing 50% cutoff of the lacunar volume cumulative distribution for diseased samples. In the larger lacunae 900-3000 μm^3 range, we found significantly higher lacunar density and microporosity in the MM group compared to the MGUS/SMM group. Regarding the shape distribution, the MGUS/SMM group showed a trend for flatter, more elongated and anisotropic osteocyte lacunae compared to the control group, though the differences were not statistically significant. Altogether, our findings suggest that osteocytes in human MM bone disease undergo changes in their lacunae morphology, which could be an indicator for impaired bone quality. Future studies are needed to show whether these are consistent within comparable anatomical sites and could serve as a diagnostic or prognostic marker.

Keywords

Osteocyte lacuna, Morphometry; High resolution microCT; Human bone biopsy; Multiple myeloma (MM); Monoclonal gammopathy of undetermined significance (MGUS); Smoldering myeloma (SMM)

1. Introduction

Bone is a dynamic organ which, besides providing structural support to the body, acts as a metabolic and hematopoietic reservoir. In addition to the vast number of cell types and biomolecules involved in the bone organ, bone extracellular matrix (ECM) also plays a crucial role in maintaining bone homeostasis [1]. Bone ECM is composed of an inorganic (hydroxyapatite mineral crystals) and an organic phase (primarily of collagen type I and proteoglycans), which provide mechanical strength. Osteocytes are bone-embedded cells, connected via dendrites in a lacuno-canalicular network (LCN). They act as local sentinels in response to external stimuli and regulate the balance between bone resorption/formation [2]. Hence, factors such as collagen, mineral crystals and osteocyte LCN affecting bone matrix organization will have an impact on bone physiology

Lacunar volume, shape and density has been shown to be influenced by changes of the surrounding environment, either mechanically or chemically, and by aging or disease. Larger lacunae have been observed after exposing mice to non-gravity [3] or after treatment with glucocorticoid to slow down bone metabolism [4]. Smaller lacunar size and density have been observed in rodent models of aging [5]. Significantly lower osteocyte lacunar volume was found in an osteoporotic rat model compared to healthy controls and the effect of different anti-resorptive drugs in intracortical microporosities was evaluated [6]. In humans, decreasing lacunar density was observed with aging, while a significantly higher density was found in osteoporotic bone compared to controls [7]. A recent study with human bone biopsy samples of healthy individuals across the life span revealed decreasing osteocyte lacunae density and porosity with aging before the peak bone mass at 30 years, which then stabilized or even increased after this age [8]. Mineralized osteocyte lacunae (micropetrosis) have been found with aging and osteoporosis, attributed to osteocyte apoptosis, which was improved with bisphosphonates [9]. Lacunar shape changes have also been associated with aging, becoming smaller and more spherical with increasing age [10]. Such osteocyte morphological changes are responsible for lower local bone tissue strains and affect bone mechanosensitivity [11]. In osteogenesis imperfecta, a higher density of osteocyte lacunae per unit volume [12–14], with more spherical shape compared to the ellipsoidal lacunae in control mice was observed [14].

In cancer, osteocytes, as well as osteoblasts and osteoclasts, communicate with tumor cells and this generates a microenvironment that supports cancer cell growth and stimulates bone destruction [15]. Interactions between breast and prostate cancer cells and osteocytes affect the

cancer cell migration and invasion potential and contribute to the establishment and progression of bone metastasis [16,17]. Also, breast cancer cells induce osteocyte apoptosis and alter osteocyte function [18]. Recently, a study of osteotropic cancers in rodents revealed that the spatial distribution of cortical bone microporosity, osteocyte lacunae volume and the LCN characteristics are influenced by the presence of tumor cells in osteosclerotic and osteolytic lesions [19]. Taken together, changes in bone microstructure and the LCN play a role in different types of bone metastasis. Ultrastructural characterization will help understand how different tumor cells interact with osteocytes, causing characteristic footprints in the bone microstructure and impairing bone integrity and physiology.

An example of an incurable malignancy of the bone marrow is multiple myeloma (MM), in which plasma cells disrupt the bone homeostasis towards excessive bone resorption [20]. Patients diagnosed with MM develop symptoms termed CRAB: hypercalcemia, renal insufficiency, anemia and osteolytic bone lesions[21]. Initially, an abnormal proliferation of plasma cells (< 10%) producing aberrant antibodies in serum (< 3 g/dL) is clinically identified as benign, termed 'monoclonal gammopathy of underdetermined significance' (MGUS). When MGUS continuously progresses into the next stage, named smoldering multiple myeloma (SMM), CRAB symptoms are not yet present. However, SMM represents a broad biological spectrum: (i) clinical cases which do not progress into symptomatic disease over years, and (ii) high-risk cases in which patients have an 80 % chance of disease progression within two years [22]. To better define those high-risk SMM, who require immediate intervention to prevent end-organ damage, particularly to bone and kidney, the International Myeloma Working Group published updated the criteria for the diagnosis of MM [23]. Validated biomarkers were included, such as the detection of one or more focal lesions by magnetic resonance imaging (MRI) and diffuse infiltration (≥ 60%) of clonal plasma cell in the bone marrow even without bone lytic lesions.

MM cells alter the bone marrow environment by releasing signals that promote osteoclast activity, while inhibiting osteoblast function [24,25]. Interestingly, MM bone lesions rarely heal, even after years of patients being in complete disease remission [26]. There is evidence that MM cells also target osteocytes by enhancing cell apoptosis and expression of sclerostin, an inhibitor of bone formation [27]. Even though MM cells directly interact with osteocytes and vice versa, the consequences of these interactions on the local bone microstructure and the role of the ECM in disease development are largely unknown [27]. Our group has shown local

ECM alterations with active erosion sites, irregular shaped osteocyte lacunae and altered osteocyte LCN architecture, using an early MM mouse model [28]. Thus, examining the bone microstructure in MM and the precursor conditions MGUS and SMM would provide insights in the pathophysiology of this disease. It is currently unknown how human bone ECM is affected at the ultrastructural level in MGUS, SMM and newly diagnosed MM bone disease. The aim of this study is to quantitatively characterize changes in osteocyte lacunae and micropores from MGUS to newly diagnosed MM, using ex vivo human bone biopsies. Determination of these changes could help identifying diagnostic or prognostic indicators for the progression of MM bone disease.

2. Results

2.1 Clinical data and patient history

Clinical data from patients from the University Hospital Würzburg and parameters describing bone metabolism are compiled in Tables 1-3. The cohort included patient-derived bone biopsy samples with the precursor condition MGUS (Table 1), SMM (Table 2), and newly diagnosed MM (Table 3). The revised International Staging System for Multiple myeloma (r-ISS) was used to stratify patients with respect to their survival [29]. Control samples obtained from the University Hospital Würzburg and from the Ludwig Boltzmann-Institute of Osteology Vienna are compiled in Table 4. Only biopsy samples containing sufficient trabecular bone were included.

Patients with MGUS showed no detectable osteolytic bone lesions by low-dose CT scans. One patient with MGUS received denosumab for four months. In this case, we cannot exclude that the anti-resorptive treatment interfered with the bone ultrastructure. Similarly, the two patients classified as SMM exhibited no signs of osteolytic lesions by low-dose CT scans at the time of biopsy. The disease stage of SMM was based on the percent of bone marrow infiltration of $CD138^+$ cells, above 10%. Patients classified as MM had a bone marrow infiltration of $CD138^+$ cells between 60-90% (4 out of 6), a ratio of the involved to the uninvolved free light chain in the serum (sFLC) of >100 (2 out of 6), and/or local or disseminated lytic lesions, as well as reduced bone mineral density (4 out of 6). All bone turnover markers (phosphate, calcium, alkaline phosphatase) were within normal ranges. Anti-resorptive therapy with the bisphosphonate zoledronic acid had been administered to one MM patient for one month before the biopsy was taken. We assume that the single dose of the bisphosphonate did not affect bone ultrastructure in such short time.

2.2 Immunohistochemical (IHC) and microcomputed tomography (microCT) overview analysis

As part of the standard clinical practice, bone biopsies were processed for immunohistochemical (IHC) analysis for CD138 staining, to detect the clonal bone marrow plasma cells and quantify the percent of bone marrow infiltration of $CD138^+$ cells. Fig. 1a-c shows representative samples of MGUS, SMM and newly diagnosed MM patients with <10% for MGUS and >10% for SMM and MM patients. Bone biopsy samples containing sufficient trabecular bone were scanned with microcomputed tomography (microCT). 3D renders of representative images are shown in Fig. 1d-f. Quantification of trabecular thickness distribution is shown in Fig. 1g-j. No differences between the three groups were observed in the macroscopic trabecular bone architecture, indicating the resolution might limit the ability to detect pathological changes.

2.3 Bone ultrastructure and segmentation of osteocyte lacunar microporosity

We next investigated the bone ultrastructure with a focus on the osteocyte lacunar microporosity. High resolution microCT scans (voxel size 1-2 μm) were performed on smaller volumes of interest (VOI) and the empty cavities within mineralized tissue corresponding to osteocyte lacunae were segmented. Cavities smaller than 20 μm^3 and larger than 3000 μm^3 were considered cracks or artifacts and excluded from the analysis. VOI of representative samples and the segmented osteocyte lacunar microporosity are visualized in Fig. 2.

2.4. Osteocyte lacunar volume distribution and microporosity analysis

We characterized the osteocyte lacunar volume distribution, first as a frequency distribution (Fig. 3) and then as a cumulative distribution (Fig. 4). To plot the lacunar volume frequency distribution, all lacunae within one sample were stratified according to volume intervals. For a discrete lacunar volume interval, we quantified the number of osteocyte lacunae (Lc.N.) for that given size, normalized to the trabecular bone volume and excluding lacunar total volume (Tb.TV-Lc.TV), to account for samples of different size. Two separate lacunar volume ranges were investigated: small lacunae 20-900 μm^3 (Fig. 3a-c) and larger lacunae 900-3000 μm^3 (Fig. 3d-f). Control samples (Fig. 3a, d) were compared with MGUS, SMM (Fig. 3b, e), and MM (Fig. 3c, f).

In the small lacunae range 20-900 μm^3, we observed a comparable distribution in the different groups, with the exception of sample #MM 3, with significantly higher number of osteocyte lacunae compared to other samples within the MM group (Fig. 3c). In contrast, in the larger lacunae range 900-3000 μm^3, we observe a significantly higher number of lacunae for the MM group (Fig. 3f) compared with MGUS (Fig. 3d) and SMM (Fig. 3e) groups

When comparing both ranges, we observed a larger number of small osteocyte lacunae (Fig. 3a-c) compared to larger lacunae (Fig. 3d-f). This motivated a more detailed lacunar volume cumulative distribution analysis (Fig. 4), where the lacunar number (Lc.N) was plotted as a cumulative curve. The 50% cutoff indicates that half of all osteocyte lacunae within one sample are below that specific volume interval (x-axis). In the control group (Fig. 4a), the 50% cutoff is heterogeneous: samples #control 1, #control 3 and #control 4 have 50% of the lacunae with volumes around 140-170 μm^3, while sample #control 2 has the highest volume with 270 μm^3. In the MGUS/SMM group (Fig. 4b), the 50% cutoff ranges from 170-210 μm^3, except sample #SMM 2 with the smallest cutoff at 140 μm^3. In the MM group (Fig. 4c), the 50% cutoff varies from 150-220 μm^3, with clearly lower values for the biopsies of patients without bone osteolytic lesions (#MM 3 and #MM 6). In conclusion, we observe a trend for increasing 50% cutoff for more advanced disease, indicating that the sum volume of the smallest 50% lacunae account for a larger volume as the disease progresses (Fig. 4c).

Finally, we calculated the lacunar density as the total number of osteocyte lacunae (Lc.TN) normalized to the trabecular bone volume and excluding lacunar total volume (Tb.TV-Lc.TV), in other words, the summation of the osteocyte lacunar volume frequency distribution (Fig. 3). This was done for both ranges separately, small lacunae 20-900 μm^3 (Fig. 5a) and larger lacunae 900-3000 μm^3 (Fig. 5b). In the small lacunae range, the mean for the control samples was 29809 +/- 11314 lacunae/mm^3, for MGUS/SMM 18165 +/- 3278 lacunae/mm^3 and for MM 20502 +/- 13827 lacunae/mm^3. No significant differences were observed in the small lacunae range, although there was a clear trend for lower lacunar density for diseased samples (MGUS/SMM and MM) compared to the controls. However, in the larger lacunae range 900-3000 μm^3 (Fig. 5b), significantly higher lacunar density was found in the MM group compared to the MGUS/SMM group.

We also calculated the microporosity as the lacunar total volume (Lc.TV) divided by trabecular total bone volume (Tb.TV) for each group. This was done for both ranges separately, small lacunae 20-900 µm³ (Fig. 5c) and larger lacunae 900-3000 µm³ (Fig. 5d). No significant differences were observed in the small lacunae range. However, in the larger lacunae range, significantly higher microporosity was found in the MM group compared to the MGUS/SMM group. This is consistent with the observations of lacunar volume frequency distribution (Fig. 3f) and lacunar density (Fig. 5b).

2.5 Osteocyte lacunar morphological analysis

We performed a lacunar morphological analysis in the small lacunae 20-900 µm³ range, for each group control, MGUS/SMM and newly diagnosed MM. Based on previous analogous analysis [30,31], we investigated the distribution of lacunar flatness, elongation and anisotropy. To do so, the principal eigenvalues for each osteocyte lacunae were obtained: EV1, EV2 and EV3. The morphological parameters were calculated as follows: lacuna elongation as EV2/EV1 (ratio of medium to largest eigenvalue) ranging from lower values for elongated and 1 for spherical (Fig. 6a-d); lacuna flatness as EV3/EV2 (ratio of smallest to medium eigenvalue) ranging from 0 for flat to 1 for spherical (Fig. 6e-h); and lacuna anisotropy as 1-EV3/EV1 (one minus the ratio of smallest to largest eigenvalue) ranging from 0 for isotropic/spherical to 1 for highest anisotropy (Fig. 6i-l). The fraction of lacunar number (Lc.N) normalized against lacunae total number (Lc.TN) in each sample is shown for each group control (Fig. 6a, e, i), MGUS/SMM (Fig. 6b, f, j) and MM (Fig. 6c, g, k). The median of all lacuna elongation values for each sample are shown in Fig. 6d; similarly, for flatness in Fig. 6h and anisotropy in Fig. 6l.

Lacuna flatness in MGUS/SMM and newly diagnosed MM groups exhibit a broader spread of the distribution compared to the control group, with a shift towards lower values (flatter shapes). Regarding lacuna elongation and anisotropy, the spread of the distribution for the three groups is comparable. A trend for lower values for lacuna elongation (more elongated) and higher values for lacuna anisotropy (more anisotropic) is observed in the MGUS/SMM group compared to the control group, as shown by the curves and the by the median values. However, the differences of the median values are not significant.

3. Discussion

Osteocyte function is altered in skeletal disorders including cancer. In MM bone disease, osteolytic lesions are frequently diagnosed in clinical CT scans, however, changes in the mineralized ECM and morphometric analyses of bone microporosity in bone biopsies are not routinely analyzed. To our knowledge, here we present the first quantitative investigation of osteocyte lacunae volume and shape distribution in human bone biopsy samples obtained from MGUS, SMM and newly diagnosed MM patients using high resolution microCT (voxel size 1-2 μm).

Our data demonstrate altered lacunae volume and shape distribution with MGUS, SMM and newly diagnosed MM. Specifically, we found a significantly higher number of larger lacunae in the 900-3000 μm^3 range in the MM group compared to the MGUS/SMM groups, as reflected in an increase in lacunar volume frequency distribution (Fig. 3f) and lacunar density (Fig. 5b). The study also found significantly higher microporosity for the larger lacunae range in the MM group compared to the MGUS/SMM group (Fig. d), consistent with the observation of an increase in lacunar volume frequency distribution. One limitation of this analysis is that the larger lacunae in the 900-3000 μm^3 range probably includes both enlarged osteocyte lacunae and other pathological features in the form of micropores.

In the small lacunae 20-900 μm^3 range, the lacunar density for control samples with 29809 +/- 11314 lacunae/mm^3 (Fig. 5a) is in the range previously reported in the literature for 3D analysis of osteocyte morphometry in healthy transiliac bone biopsies [32], which confirms the validity of our analysis. Interestingly, there was a trend for lower lacunar density for diseased samples (MGUS/SMM and MM) compared to the controls, though the differences were not significant (Fig. 5a). This could be indicative of micropetrosis, i.e. osteocyte lacunae mineralization following osteocyte apoptosis [33,34]. Since a lower lacunar density can distinguish healthy, osteoporotic and bisphosphonate-treated osteoporotic patients, it is currently being considered as a novel bone microstructural maker of impaired bone quality [33]. Finally, we observed a trend for increasing values of the 50% cutoff in the lacunar volume cumulative distribution for more advanced disease, showing that the sum volume of the smallest 50% lacunae account for a larger volume as the disease progresses (Fig. 4).

In terms of shape distribution, the MGUS/SMM group showed a trend for lower lacuna flatness (flatter), lower lacuna elongation (more elongated), and higher lacuna anisotropy

(more anisotropy) compared to the control group (Fig. 6). Altogether, the findings of a trend for lower lacunar density and increasing 50% cutoff of the lacunar volume cumulative distribution for diseased samples in the small lacunae 20-900 μm^3 range, together with significantly higher lacunar density and microporosity for the MM group in the larger lacunae 900-3000 μm^3 range, suggest that the osteocytes in MM bone disease and the precursor conditions MGUS/SMM are undergoing changes in their lacunae morphology.

In a recent study in immunocompetent mice, breast and prostate cancer cells were intratibially injected and the changes in the osteocyte LCN induced by tumor cells were analyzed by histology, microCT imaging and confocal laser scanning microscopy [27]. Interestingly, large lacunae and vascular canals were not observed in the proximity of osteolytic lesions, whereas these changes occurred in osteosclerotic lesions adjacent to prostate cancer cells [27], indicating that changes of osteocyte LCN characteristics are tumor type-specific. In our study of biopsy samples from patients with MM and the precursor conditions, we observed a significantly higher number of larger lacunae in the MM group compared to the MGUS/SMM groups. These changes may be related to the presence of osteocytic osteolysis [35], a process that involves osteocytes mobilizing calcium and phosphate, using carbonic anhydrase and vacuolar ATPase to demineralize the bone matrix, and digest protein using matrix metalloproteases and tartrate-resistant acid phosphatase (TRAP) [27,36–38]. In the above-mentioned mouse model [27], TRAP-positive osteocytes in combination with large lacunae were detected in osteosclerotic regions of breast and prostate infiltrated bones, indicating that this mechanism could contribute to the observed increase in lacunae volume [27,36–38]. Whether osteocytic osteolysis plays a role in the progression from healthy to MGUS/SMM to MM bone is not known and warrants further studies. Moreover, since the osteocyte remodeling function affects the lacunae morphology and the LCN architecture, it is likely that changes in the latter are indicators for impaired bone remodeling activity.

In order to understand the implications of altered lacunae volume and shape distribution in MM, future studies should consider several factors. First, there is a need for more bone biopsies of sufficient quality to obtain a larger sample size and validate the findings of this study. Second, it is important that the bone biopsies are obtained from comparable anatomical sites to minimize the natural osteocyte volume and shape variation within healthy bone [8,32,39]. Additionally, to further investigate the relationship between osteocyte lacunae and MM,

researchers should increase the volume of interest scanned at high resolution (1 µm voxel size or lower) for instance using phase-contrast synchrotron microCT. Furthermore, the implementation of deep learning algorithms could facilitate the analysis of large numbers of osteocyte lacunae and improve the accuracy of image analysis. In addition to lacunar abnormalities, quantitative analysis of alterations in the LCN (i.e. canalicular density, connectivity) should be explored in future studies. Finally, investigating clinical bone endocrine parameters such as parathyroid hormone, bone-specific alkaline phosphatase, amino-terminal pro-peptide of type I procollagen, carboxy-terminal telopeptide of type I collagen, TRAP5b or fibroblast growth factor-23 produced by osteocytes, in relation to calcium and phosphorus and in relation to lacunae morphology, could provide valuable insights into the pathogenesis of MM and link this to the clinical setting [40]. Measuring serum parameters may be easier than performing microCT analysis of osteocyte lacuna, and incorporating these measurements into future studies could provide a more comprehensive understanding of the impaired bone remodeling capacity in MM bone disease. Additionally, the use of animal models of MM and other bone diseases may provide a valuable tool for investigating the mechanisms underlying the observed alterations in osteocyte lacunae morphology and other aspects of bone ultrastructure, such as LCN architecture, bone composition, and micro- and nanoscale organization of the organic and inorganic matrix. We recently established a MM bone disease model for ultrastructural characterization of the ECM in early stages of the disease [28,41–43]. In skeletally mature mice, we detected a disorganized osteocyte LCN architecture, and irregular-shaped osteocyte lacunae in MM-injected bones after 21 days [28]. This model will help to characterize early on the development and progression of ultrastructural changes of MM bone disease.

Taken together, these findings suggest that altered lacunae volume and shape distribution may play a role in the pathogenesis of MM and the precursor conditions MGUS and SMM, and could potentially serve as a diagnostic or prognostic marker for the disease. Further studies are needed to explore the clinical implications of these results and to determine whether targeting lacunar abnormalities could be a viable therapeutic approach for MM.

4. Materials and methods

4.1 Patient sample collection and clinical evaluation

The purpose of this study was to determine whether changes in osteocyte lacunae volume and shape distribution could be detected in mineralized bone biopsy samples from patients with

MGUS, SMM and newly diagnosed MM. MGUS (n=3), SMM (n=2) and symptomatic MM (n=6) were diagnosed following the revised international staging system [23]. Clinical data from patients including reports of the low-dose CT scans are given in Tables 1-3. The investigators who performed the bench studies were blind to the patient information. This study was approved by the Ethics Committee of the University of Würzburg, Germany (82/20-am).

As control bone biopsy samples, two different data sets were used (Table 4). One Jamshidi bone biopsy sample (2 mm diameter) was obtained from a patient of the University Hospital Würzburg with myelodysplastic syndrome. Three samples (5 mm diameter) were obtained from an earlier study [8] from autopsies at the Ludwig Boltzmann-Institute of Osteology Vienna. Osteocyte lacunae characteristics were re-evaluated in the current study. For all control and disease bone biopsy samples, the trabecular bone compartment was analyzed and the cortical bone was excluded. Only biopsy samples containing sufficient trabecular bone were considered.

The patient clinical data (Tables 1-3) include: biopsy number, disease stage (MGUS, SMM or newly diagnosed MM), age, gender, immunoglobulin subtypes (heavy and light chains) secreted by malignant plasma cells, revised International Staging System (r-ISS), cytogenetic risk, M-protein secreted by plasma cells at time of diagnosis (g/L), heavy chain (mg/dL), involved serum free light chain (sFLC) (mg/L), ratio (involved/uninvolved sFLC), bone marrow infiltration (%) based on immunohistochemistry Syndecan-1 (CD138) with >60% corresponding to newly diagnosed MM, computed tomography findings of osteolytic lesions, hemoglobin (g/dL), creatinine (mg/dL) and cytogenetic alterations by fluorescence in situ hybridization (FISH), which allows for detection of genetic changes which are relevant for the ISS stage. In addition, parameters describing the bone metabolism include: calcium (mmol/L), alkaline phosphatase (U/L), phosphate (mmol/L) and finally, bone anti-resorption treatment ongoing at the time of biopsy.

4.2 Immunohistochemical detection of CD138 on decalcified bone paraffin sections

Paraffin embedded human specimens were retrospectively collected from formalin-fixed paraffin-embedded tissue of anonymized samples, archived at the Institute of Pathology, University of Würzburg. Shortly, Jamshidi bone biopsy samples that were derived from the clinical department of the University of Würzburg were fixed for 24 h in formalin,

decalcified for 24 h at 37°C using an EDTA-based approach, dehydrated with alcohol and xylene and then embedded in paraffin.

For the immunohistochemical detection of CD138/Syndecan-1 expression, sections were deparaffinized. The tissue was hybridized with an antibody against CD138/Syndecan-1 (clone MI15, mouse, #M7228, Agilent, Santa Clara, CA, USA), following standard procedures by automated processing using the Tecan Evo Freedom stainer and the Dako Advance system according to the manufacturer's protocol.

4.3 Microcomputed tomography (microCT): image acquisition

Specimens were scanned using an EasyTom micro/nano tomograph (RX solutions, France). Low resolution scanning parameters were: 107 kV, 93 µA, 7 µm voxel size, frame rate of 3, average frame of 5. High resolution scanning parameters were: 60 kV, 124 µA, 1-2 µm voxel size, frame rate of 1, average frame of 5. Reconstruction of the 1120 projections/scan were performed using RX Solutions X-Act software.

4.4 Low resolution microCT: image analysis

The overall bone biopsy morphology with particular focus on trabecular bone thickness was analyzed with Dragonfly v.2022.1 software (Object Research Systems Inc., Montreal, Canada, 2022). Low resolution microCT stack images (voxel size of 7 µm) were segmented using Otsu thresholding ("denoising" of these microCT images and objects was not necessary). A mesh was then created from each individual region of interest (ROI) of the trabecular bone.

The trabecular bone strut thickness was automatically measured from each mesh by Dragonfly software. For this, we calculated the mean and standard deviation values of about 3-5.5 10^6 local vertices created between boundary points of each overall mesh. The software calculated these vertices as diameters of hypothetical spheres that fit within each boundary points of the mesh. The trabecular bone strut thickness distribution is depicted with a color code for each biopsy and as a histogram.

4.5 High resolution microCT: image analysis

<u>4.5.1 Segmentation of osteocyte lacunae</u>

The stack of high resolution microCT images (1-2 µm voxel size) was segmented using Otsu thresholding in Dragonfly. For these images, noise removal was performed using 3D smoothing (kernel of 3) as morphological operation. Next, the binary mask was used to extract the pores. Osteocyte lacunae were filled in a copy of the binary mask using a filling morphological operation. Next, the multi-ROI conversion tool of Dragonfly was used to select each lacuna individually. This tool allowed to define each osteocyte lacuna as an individual ROI, hence enabling the calculation of each lacunae volume and shape. The generated binary images were then used for the quantitative analysis of lacunae volume and shape with Python software (version 3.5). The script used was written in a Jupyter notebook with Python software (version 3.7). External libraries not contained in the Anaconda environment were installed from their repository. Micropores smaller than 20 μm^3 and larger than 3000 μm^3 were considered cracks or artifacts and excluded from the analysis. Two separate lacunar volume ranges were investigated: small lacunae 20-900 μm^3 [44] and larger lacunae 900-3000 μm^3.

4.5.2 Osteocyte lacunar volume analysis

For the osteocyte lacunar volume analysis, each segmented lacunar volume was calculated as the total number of voxels times the volume of a single voxel. Based on this, we could define the number of lacunae (Lc.N) of a given lacunar volume (Lc.V). We could also define the total number of osteocyte lacunae (Lc.TN), total lacunar volume (Lc.TV) and trabecular bone volume (Tb.BV). This nomenclature and units are summarized in Table 5.

4.5.3 Normalized lacunar volume frequency distribution and lacunar density

The lacunar volume frequency distributions were normalized to the trabecular bone volume to account for size differences between samples, since larger samples have more lacunae than smaller ones. For a given lacunar volume (Lc.V), we quantified the lacunar number (Lc.N), normalized to the trabecular bone volume (Tb.BV) and excluding the total lacunar volume (Tb.TV-Lc.TV). The data is presented as the frequency in a histogram with a bin size of 20 μm^3. Furthermore, the lacunar density was calculated as the total number of osteocyte lacunae (Lc.TN) normalized to the trabecular bone volume and excluding lacunar total volume (Tb.TV-Lc.TV), in other words, the summation of the osteocyte lacunar volume frequency distribution. This was done for both ranges separately, small lacunae 20-900 μm^3 and larger lacunae 900-3000 μm^3.

4.5.4 Lacunar volume cumulative distribution

The cumulative distribution is calculated by sorting all osteocyte lacunae by volume, from smallest to largest, and increasing the count of the fraction 1/N at each point, with N = length of array. The cumulative lacunae volume distribution was plotted with respect to the lacunae volume (Lc.V), with the x axis showing a given lacunae volume and the y axis showing the cumulative volume. The 50% cutoff illustrating the specific volume below which half of all osteocyte lacunae are contained, was marked with a dashed line.

4.5.5 Osteocyte lacunar microporosity analysis

The microporosity was calculated as the lacunar total volume (Lc.TV) divided by trabecular total bone volume (Tb.TV) for each group. This was done for both ranges separately, small lacunae 20-900 μm^3 and larger lacunae 900-3000 μm^3.

4.5.6 Osteocyte lacunar morphological analysis

To perform the lacunar morphological analysis, we defined the eigenvectors of an individual lacuna with the corresponding major and minor axes. From the eigenvectors, the corresponding eigenvalues (EV) were derived (EV1 > EV2 > EV3), where EV1 is the largest eigenvalue and EV3 the smallest [45,46]. Three parameters were assessed to examine lacunae morphology, based on the eigenvalues of each individual lacuna: the lacuna elongation, flatness and anisotropy [30,31]. This nomenclature and units are summarized in Table 6.

4.6 Statistical analysis

A total of n=15 bone biopsy samples were analyzed, including MGUS n=3, SMM n=2, newly diagnosed MM n=6 and control biopsy samples n=4 (Jamshidi n=1 and from autopsies n=3). Additional bone biopsy samples (n>15) were collected but excluded from the analysis due to lack of sample integrity (e.g. loss of bone structure (bone debris) during the extraction procedure) or insufficient trabecular bone. To analyze changes in bone microporosity and lacunar morphological analysis, a one-way analysis of variance (ANOVA) with Tukey's multiple comparisons test (*$p<0.05$) was used (GraphPad Prism 8.0 software).

5. Conflict of interest

The authors declare no conflict of interest.

6. Data availability

The raw/processed data required to reproduce these findings are available in a publicly accessible repository of the Max Planck Society.

7. Author contributions

A Cipitria, I. Moreno-Jiménez and F. Jundt conceived the idea. I. Moreno-Jiménez and S. Heinig processed the bone biopsy samples and performed the experiments. D. Maichl collected and prepared the human Jamshidi bone biopsy samples. S. Strifler educated patients about and performed the biopsies, and collected clinical data. E. Leich-Zbat collected the human bone biopsy samples and clinical data; S. Blouin provided the control bone autopsy samples. I. Moreno-Jiménez, S. Heinig, U. Heras, F. Jundt and A. Cipitria analyzed the data. P. Fratzl and N. Fratzl-Zelman together with A Cipitria, I. Moreno-Jiménez and F. Jundt evaluated the methods and results. A Cipitria, I. Moreno-Jiménez and F. Jundt drafted the manuscript. All authors discussed the results and contributed to the final manuscript.

8. Funding

This research was funded by a postdoctoral research fellowship from the Humboldt Foundation (I.M.-J.) and by the Deutsche Forschungsgemeinschaft (DFG) Emmy Noether grant CI 203/2-1 (A.C). This work was supported by the Interdisciplinary Center for Clinical Research (IZKF), Medical Faculty of Würzburg, grant B-409 (F.J.) and the German Research Foundation (DFG) grants JU426/10-1 (F.J., 491715122) and JU 426/11-1 (F.J., 496963451). A.C. also thanks the funding from IKERBASQUE Basque Foundation for Science and from the Spanish Ministry of Science and Innovation (PID2021-123013OB-I00) (Ministerio de Ciencia e Innovación, la Agencia y del Fondo Europeo de Desarrollo Regional, Proyecto PID2021-123013OB-I00 financiado por MCIN/AEI/10.13039/501100011033/FEDER.UE).

9. Acknowledgements

The authors thank Daniel Werner, Jeannette Steffen, Daniela Garske and Susann Weichold at the Max Planck Institute of Colloids and Interfaces in Potsdam for their technical assistance.

References

1. Fratzl, P. & Weinkamer, R. Nature's hierarchical materials. *Prog Mater Sci* **52,** 1263–1334 (2007).
2. Bonewald, L. F. The amazing osteocyte. *Journal of Bone and Mineral Research* **26,** 229–238 (2011).

3. Gerbaix, M., Gnyubkin, V., Farlay, D., Olivier, C., Ammann, P., Courbon, G., Laroche, N., Genthial, R., Follet, H., Peyrin, F., Shenkman, B., Gauquelin-Koch, G. & Vico, L. One-month spaceflight compromises the bone microstructure, tissue-level mechanical properties, osteocyte survival and lacunae volume in mature mice skeletons. *Sci Rep* **7,** 2659 (2017).
4. Lane, N. E., Yao, W., Balooch, M., Nalla, R. K., Balooch, G., Habelitz, S., Kinney, J. H. & Bonewald, L. F. Glucocorticoid-treated mice have localized changes in trabecular bone material properties and osteocyte lacunar size that are not observed in placebo-treated or estrogen-deficient mice. *Journal of Bone and Mineral Research* **21,** 466–476 (2005).
5. Tiede-Lewis, L. M. & Dallas, S. L. Changes in the osteocyte lacunocanalicular network with aging. *Bone* **122,** 101–113 (2019).
6. Tommasini, S. M., Trinward, A., Acerbo, A. S., De Carlo, F., Miller, L. M. & Judex, S. Changes in intracortical microporosities induced by pharmaceutical treatment of osteoporosis as detected by high resolution micro-CT. *Bone* **50,** 596–604 (2012).
7. Mullender, M. G., van der Meer, D. D., Huiskes, R. & Lips, P. Osteocyte density changes in aging and osteoporosis. *Bone* **18,** 109–113 (1996).
8. Blouin, S., Misof, B. M., Mähr, M., Fratzl-Zelman, N., Roschger, P., Lueger, S., Messmer, P., Keplinger, P., Rauch, F., Glorieux, F. H., Berzlanovich, A., Gruber, G. M., Brugger, P. C., Shane, E., Recker, R. R., Zwerina, J. & Hartmann, M. A. Osteocyte lacunae in transiliac bone biopsy samples across life span. *Acta Biomater* **157,** 275–287 (2023).
9. Milovanovic, P., Zimmermann, E. A., Riedel, C., Scheidt, A. vom, Herzog, L., Krause, M., Djonic, D., Djuric, M., Püschel, K., Amling, M., Ritchie, R. O. & Busse, B. Multi-level characterization of human femoral cortices and their underlying osteocyte network reveal trends in quality of young, aged, osteoporotic and antiresorptive-treated bone. *Biomaterials* **45,** 46–55 (2015).
10. Hemmatian, H., Bakker, A. D., Klein-Nulend, J. & van Lenthe, G. H. Aging, osteocytes, and mechanotransduction. *Curr Osteoporos Rep* **15,** 401–411 (2017).
11. Hemmatian, H., Bakker, A. D., Klein-Nulend, J. & van Lenthe, G. H. Alterations in osteocyte lacunar morphology affect local bone tissue strains. *J Mech Behav Biomed Mater* **123,** 104730 (2021).
12. Mähr, M., Blouin, S., Behanova, M., Misof, B. M., Glorieux, F. H., Zwerina, J., Rauch, F., Hartmann, M. A. & Fratzl-Zelman, N. Increased Osteocyte Lacunae Density in the Hypermineralized Bone Matrix of Children with Osteogenesis Imperfecta Type I. *Int J Mol Sci* **22,** 4508 (2021).
13. Hedjazi, G., Guterman-Ram, G., Blouin, S., Schemenz, V., Wagermaier, W., Fratzl, P., Hartmann, M. A., Zwerina, J., Fratzl-Zelman, N. & Marini, J. C. Alterations of bone material properties in growing Ifitm5/BRIL p.S42 knock-in mice, a new model for atypical type VI osteogenesis imperfecta. *Bone* **162,** 116451 (2022).
14. Carriero, A., Doube, M., Vogt, M., Busse, B., Zustin, J., Levchuk, A., Schneider, P., Müller, R. & Shefelbine, S. J. Altered lacunar and vascular porosity in osteogenesis imperfecta mouse bone as revealed by synchrotron tomography contributes to bone fragility. *Bone* **61,** 116–124 (2014).
15. Atkinson, E. G. & Delgado-Calle, J. The emerging role of osteocytes in cancer in bone. *JBMR Plus* **3,** e10186 (2019).
16. Adhikari, M. & Delgado-Calle, J. Role of osteocytes in cancer progression in the bone and the associated skeletal disease. *Curr Osteoporos Rep* **19,** 247–255 (2021).

17. Hofbauer, L. C., Bozec, A., Rauner, M., Jakob, F., Perner, S. & Pantel, K. Novel approaches to target the microenvironment of bone metastasis. *Nat Rev Clin Oncol* **18,** 488–505 (2021).
18. Mastro, A. M., Gay, C. V., Welch, D. R., Donahue, H. J., Jewell, J., Mercer, R., DiGirolamo, D., Chislock, E. M. & Guttridge, K. Breast cancer cells induce osteoblast apoptosis: A possible contributor to bone degradation. *J Cell Biochem* **91,** 265–276 (2004).
19. Hemmatian, H., Conrad, S., Furesi, G., Mletzko, K., Krug, J., Faila, A. V., Kuhlmann, J. D., Rauner, M., Busse, B. & Jähn-Rickert, K. Reorganization of the osteocyte lacuno-canalicular network characteristics in tumor sites of an immunocompetent murine model of osteotropic cancers. *Bone* **152,** 116074 (2021).
20. Roodman, G. Pathogenesis of myeloma bone disease. *Blood Cells Mol Dis* **32,** 290–292 (2004).
21. Huston, A. & Roodman, G. D. Role of the microenvironment in multiple myeloma bone disease. *Future Oncology* **2,** 371–378 (2006).
22. Jacobsen, R. B. & Pharm, D. Diagnosis of smoldering multiple myeloma the TEMPI syndrome — A novel multisystem disease. *New England Journal of Medicine* 2011–2012 (2011).
23. Rajkumar, S. V., Dimopoulos, M. A., Palumbo, A., Blade, J., Merlini, G., Mateos, M.-V., Kumar, S., Hillengass, J., Kastritis, E., Richardson, P., Landgren, O., Paiva, B., Dispenzieri, A., Weiss, B., LeLeu, X., Zweegman, S., Lonial, S., Rosinol, L., Zamagni, E., Jagannath, S., Sezer, O., Kristinsson, S. Y., Caers, J., Usmani, S. Z., Lahuerta, J. J., Johnsen, H. E., Beksac, M., Cavo, M., Goldschmidt, H., Terpos, E., Kyle, R. A., Anderson, K. C., Durie, B. G. M. & Miguel, J. F. S. International myeloma working group updated criteria for the diagnosis of multiple myeloma. *Lancet Oncol* **15,** e538–e548 (2014).
24. Berenson, J., Rajdev, L. & Broder, M. Bone complications in multiple myeloma. *Cancer Biol Ther* **5,** 1082–1085 (2006).
25. Terpos, E., Ntanasis-Stathopoulos, I. & Dimopoulos, M. A. Myeloma bone disease: from biology findings to treatment approaches. *Blood* **133,** 1534–1539 (2019).
26. Callander, N. S. & Roodman, G. D. Myeloma bone disease. *Semin Hematol* **38,** 276–285 (2001).
27. Delgado-Calle, J., Anderson, J., Cregor, M. D., Hiasa, M., Chirgwin, J. M., Carlesso, N., Yoneda, T., Mohammad, K. S., Plotkin, L. I., Roodman, G. D. & Bellido, T. Bidirectional notch signaling and osteocyte-derived factors in the bone marrow microenvironment promote tumor cell proliferation and bone destruction in multiple myeloma. *Cancer Res* **76,** 1089–1100 (2016).
28. Ziouti, F., Soares, A. P., Moreno-Jiménez, I., Rack, A., Bogen, B., Cipitria, A., Zaslansky, P. & Jundt, F. An early myeloma bone disease model in skeletally mature mice as a platform for biomaterial characterization of the extracellular matrix. *J Oncol* **2020,** 1–12 (2020).
29. Palumbo, A., Avet-Loiseau, H., Oliva, S., Lokhorst, H. M., Goldschmidt, H., Rosinol, L., Richardson, P., Caltagirone, S., Lahuerta, J. J., Facon, T., Bringhen, S., Gay, F., Attal, M., Passera, R., Spencer, A., Offidani, M., Kumar, S., Musto, P., Lonial, S., Petrucci, M. T., Orlowski, R. Z., Zamagni, E., Morgan, G., Dimopoulos, M. A., Durie, B. G. M., Anderson, K. C., Sonneveld, P., San Miguel, J., Cavo, M., Rajkumar, S. V. & Moreau, P. Revised International Staging System for Multiple Myeloma: A Report From International Myeloma Working Group. *Journal of Clinical Oncology* **33,** 2863–2869 (2015).

30. El Bialy, I., Jiskoot, W. & Reza Nejadnik, M. Formulation, delivery and stability of bone morphogenetic proteins for effective bone regeneration. *Pharm Res* **34,** 1152–1170 (2017).
31. Chaumel, J., Schotte, M., Bizzarro, J. J., Zaslansky, P., Fratzl, P., Baum, D. & Dean, M. N. Co-aligned chondrocytes: Zonal morphological variation and structured arrangement of cell lacunae in tessellated cartilage. *Bone* **134,** 115264 (2020).
32. Goff, E., Cohen, A., Shane, E., Recker, R. R., Kuhn, G. & Müller, R. Large-scale osteocyte lacunar morphological analysis of transiliac bone in normal and osteoporotic premenopausal women. *Bone* **160,** 116424 (2022).
33. Milovanovic, P. & Busse, B. Phenomenon of osteocyte lacunar mineralization: indicator of former osteocyte death and a novel marker of impaired bone quality? *Endocr Connect* **9,** R70–R80 (2020).
34. Delgado-Calle, J., Bellido, T. & Roodman, G. D. Role of osteocytes in multiple myeloma bone disease. *Curr Opin Support Palliat Care* **8,** 407–413 (2014).
35. Tsourdi, E., Jähn, K., Rauner, M., Busse, B. & Bonewald, L. F. Physiological and pathological osteocytic osteolysis. *J Musculoskelet Neuronal Interact* **18,** 292–303 (2018).
36. Jähn, K., Kelkar, S., Zhao, H., Xie, Y., Tiede-Lewis, L. M., Dusevich, V., Dallas, S. L. & Bonewald, L. F. Osteocytes acidify their microenvironment in response to PTHrP in vitro and in lactating mice in vivo. *Journal of Bone and Mineral Research* **32,** 1761–1772 (2017).
37. Kogawa, M., Wijenayaka, A. R., Ormsby, R. T., Thomas, G. P., Anderson, P. H., Bonewald, L. F., Findlay, D. M. & Atkins, G. J. Sclerostin regulates release of bone mineral by osteocytes by induction of carbonic anhydrase 2. *Journal of Bone and Mineral Research* **28,** 2436–2448 (2013).
38. Tang, S. Y., Herber, R.-P., Ho, S. P. & Alliston, T. Matrix metalloproteinase-13 is required for osteocytic perilacunar remodeling and maintains bone fracture resistance. *Journal of Bone and Mineral Research* **27,** 1936–1950 (2012).
39. Schemenz, V., Gjardy, A., Chamasemani, F. F., Roschger, A., Roschger, P., Zaslansky, P., Helfen, L., Burghammer, M., Fratzl, P., Weinkamer, R., Brunner, R., Willie, B. M. & Wagermaier, W. Heterogeneity of the osteocyte lacuno-canalicular network architecture and material characteristics across different tissue types in healing bone. *J Struct Biol* **212,** 107616 (2020).
40. Vlot, M. C., den Heijer, M., de Jongh, R. T., Vervloet, M. G., Lems, W. F., de Jonge, R., Obermayer-Pietsch, B. & Heijboer, A. C. Clinical utility of bone markers in various diseases. *Bone* **114,** 215–225 (2018).
41. Schwarzer, R., Nickel, N., Godau, J., Willie, B. M., Duda, G. N., Schwarzer, R., Cirovic, B., Leutz, A., Manz, R., Bogen, B., Dörken, B. & Jundt, F. Notch pathway inhibition controls myeloma bone disease in the murine MOPC315.BM model. *Blood Cancer J* **4,** e217–e217 (2014).
42. Rummler, M., Ziouti, F., Bouchard, A. L., Brandl, A., Duda, G. N., Bogen, B., Beilhack, A., Lynch, M. E., Jundt, F. & Willie, B. M. Mechanical loading prevents bone destruction and exerts anti-tumor effects in the MOPC315.BM.Luc model of myeloma bone disease. *Acta Biomater* **119,** 247–258 (2021).
43. Ziouti, F., Rummler, M., Steyn, B., Thiele, T., Seliger, A., Duda, G. N., Bogen, B., Willie, B. M. & Jundt, F. Prevention of bone destruction by mechanical loading is not enhanced by the Bruton's tyrosine kinase inhibitor CC-292 in myeloma bone disease. *Int J Mol Sci* **22,** 3840 (2021).

44. McCreadie, B. R., Hollister, S. J., Schaffler, M. B. & Goldstein, S. A. Osteocyte lacuna size and shape in women with and without osteoporotic fracture. *J Biomech* **37,** 563–572 (2004).
45. Gescheidtova, E., Marcon, P., Bartusek, K., Gescheidtová, E., Marcon, P. & Bartusek, K. Visualization of plant fibres via diffusion tensor imaging. in *PIERS Proceedings, Suzhou, China* (2011).
46. Mader, K. S., Schneider, P., Müller, R. & Stampanoni, M. A quantitative framework for the 3D characterization of the osteocyte lacunar system. *Bone* **57,** 142–154 (2013).

Figures and captions

Figure 1

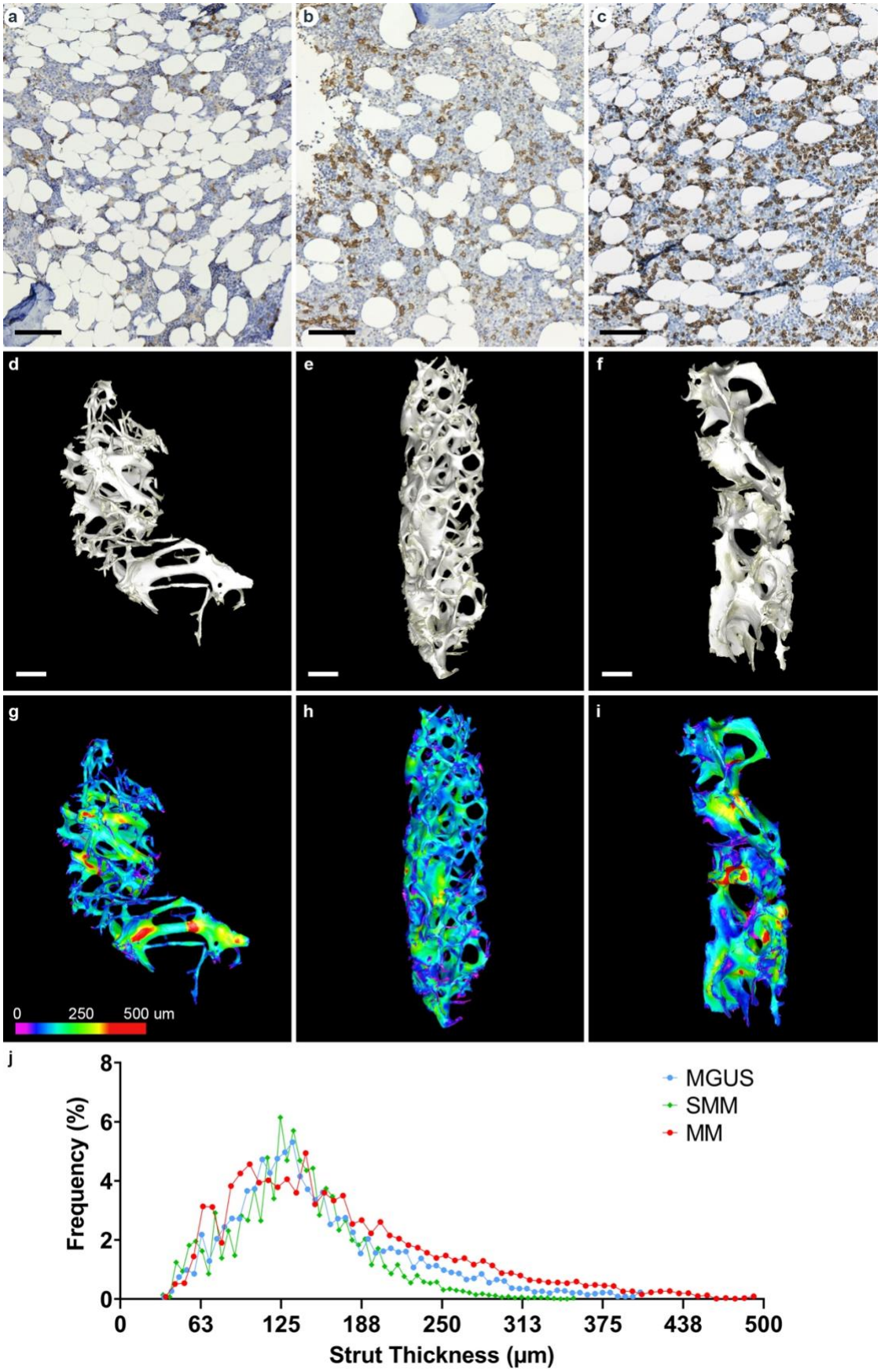

Figure 1. Immunohistochemical (IHC) CD138 staining and low resolution microCT overview of the bone biopsies from patients with: (a, d, g) monoclonal gammopathy of undetermined significance (MGUS), (b, e, h) smoldering myeloma (SMM), and (c, f, i) newly diagnosed multiple myeloma (MM). (a-c) Representative light microscopy images of the bone marrow compartment from the biopsy samples: CD138 positive staining in brown, cell nuclei counterstain in blue. (d-f) 3D renders of low resolution (7 μm voxel) microCT scans of representative bone biopsies. (g-i) Quantitative analysis of trabecular bone strut thickness distribution and color code visualization with Dragonfly software. (j) Frequency distribution of strut thickness. Scale bars equal to 100 μm (a-c), 1 mm (d-f).

Figure 2

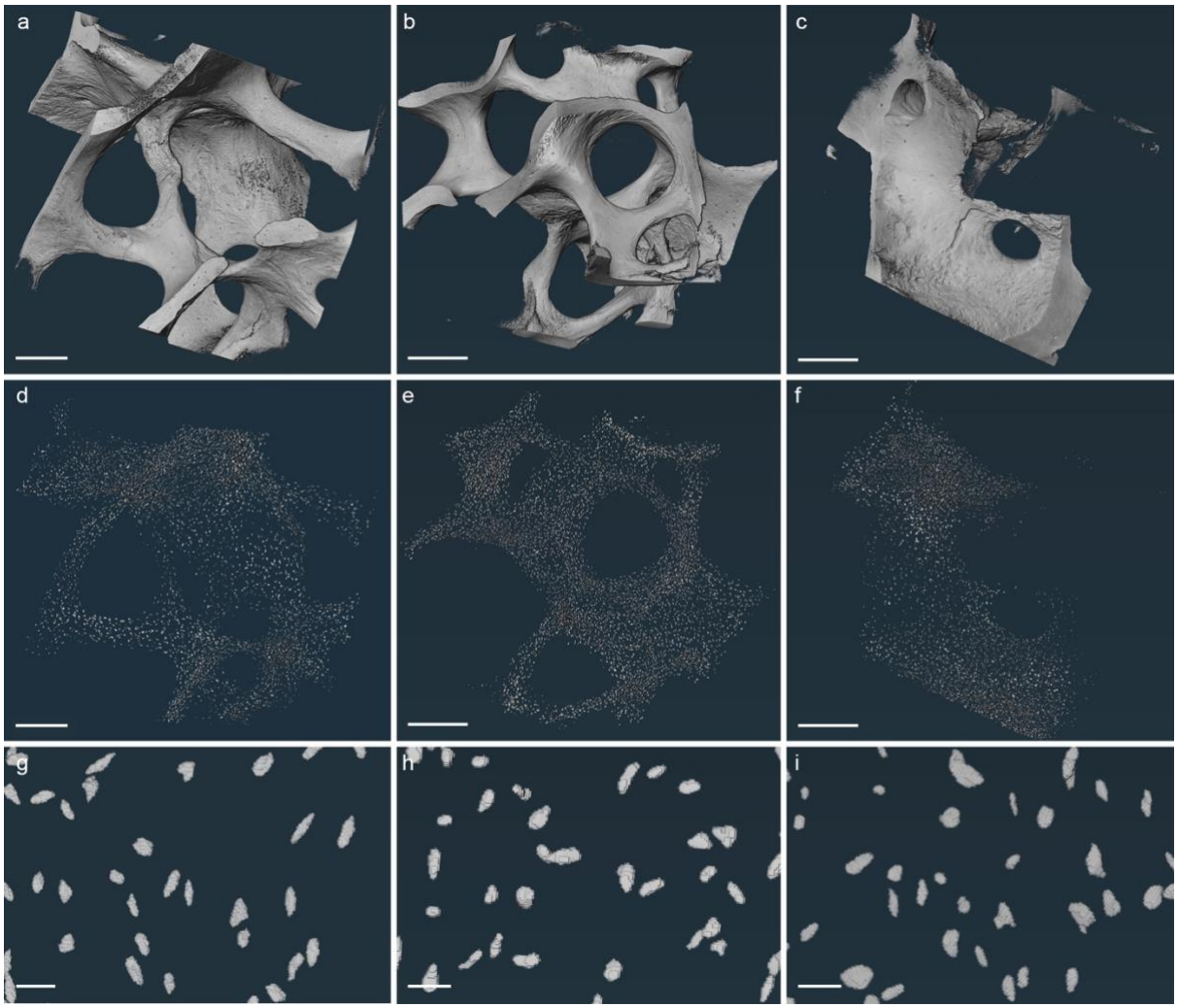

Figure 2. Bone biopsy macroscopic structure and osteocyte lacunar microporosity visualized with high resolution microCT. (a-c) 3D rendering of local scans (high resolution microCT; voxel size 1-2 μm) and (d-f) the corresponding segmented osteocyte lacunar microporosity of representative samples: (a, d, g) MGUS bone biopsy #MGUS 2, (b, e, h) SMM bone biopsy #SMM 1, (c, f, i) MM bone biopsy #MM 1. Scale bars equal to 250 μm (a, d), 350 μm (b, e), 400 μm (c, f) and 20 μm (g-i).

Figure 3

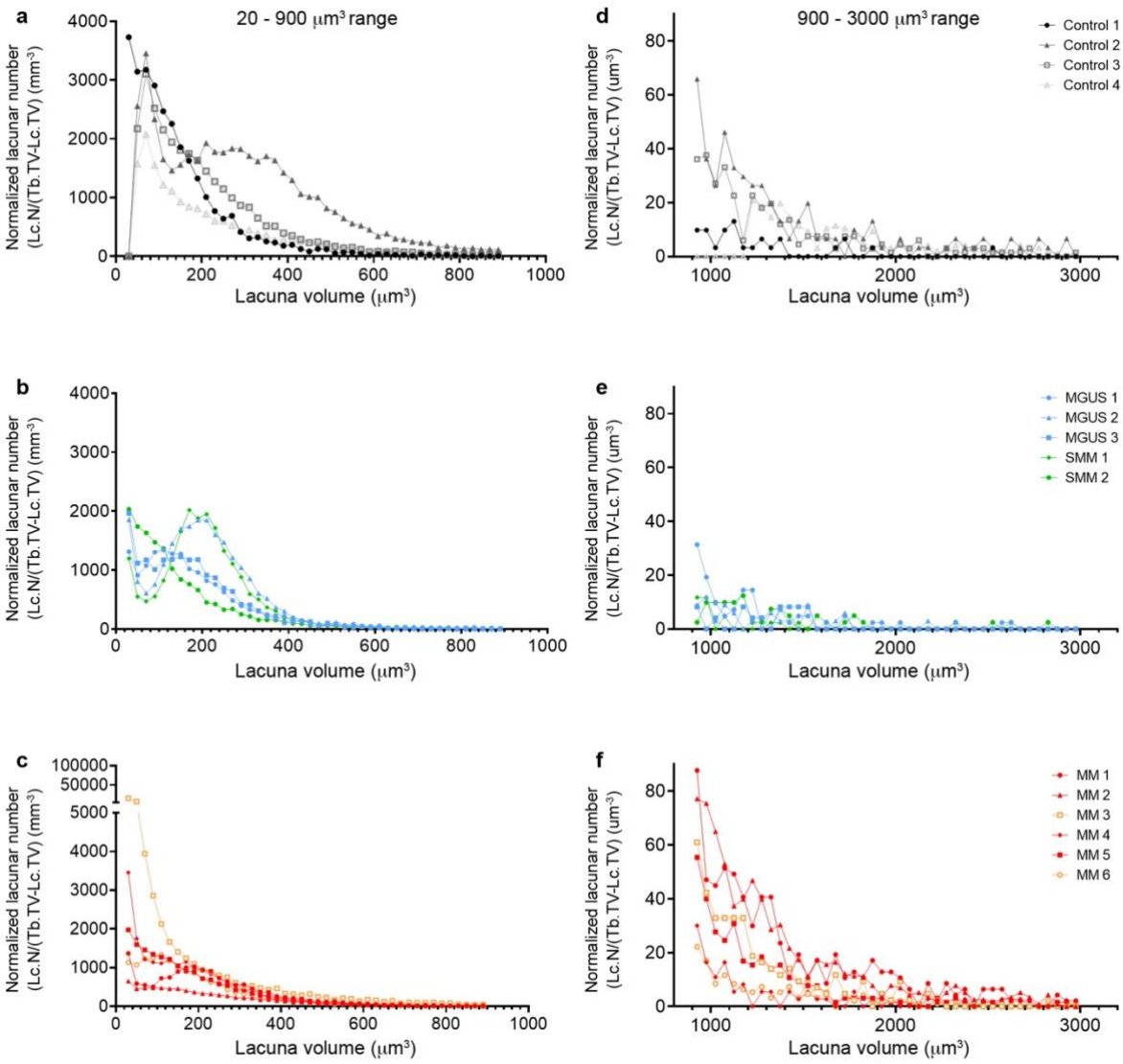

Figure 3. Lacunar volume frequency distribution. Frequency distribution normalized to trabecular bone volume for two separate lacunar volume ranges: 20-900 µm³ and 900-3000 µm³. For each lacunae volume interval (x-axis), number of osteocyte lacunae (Lc.N) normalized by the trabecular total bone volume excluding lacunar total volume (Tb.TV-Lc-TV) (y-axis). Frequency distribution for each group: (a, d) control, (b, e) MGUS and SMM, (c, f) MM. Sample from the Jamshid biopsy in black, all other control samples in grey. MGUS in blue, SMM in green, MM samples with bone lytic lesion in red, MM samples without lytic lesions in orange.

Figure 4

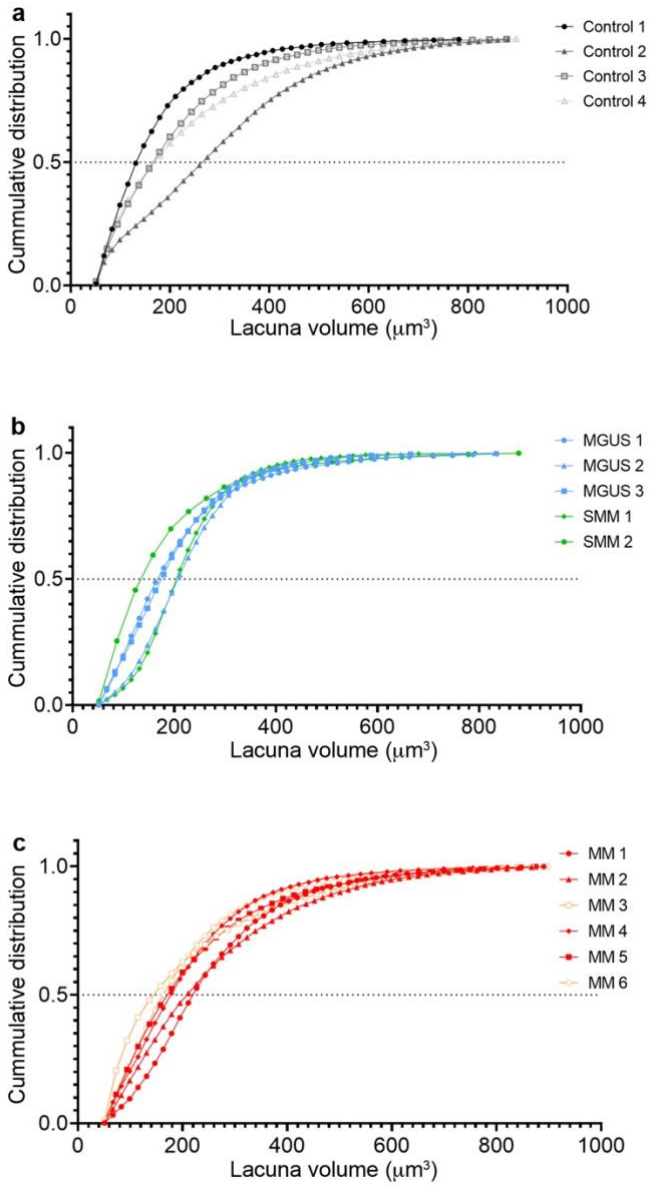

Figure 4. Lacunar volume cumulative distribution for the small lacunae 20-900 µm³ range. Cumulative distribution (from 0 to 1) of lacunae (y-axis) for each volume in µm³ (x-axis). Cumulative distribution for each group: (a) control, (b) MGUS and SMM, (c) MM. Dashed line indicates the 50% cutoff volume below which are half of all osteocyte lacunae of one sample. Sample from the Jamshid biopsy in black, all other control samples in grey. MGUS in blue, SMM in green, MM samples with bone lytic lesion in red, MM samples without lytic lesions in orange.

Figure 5

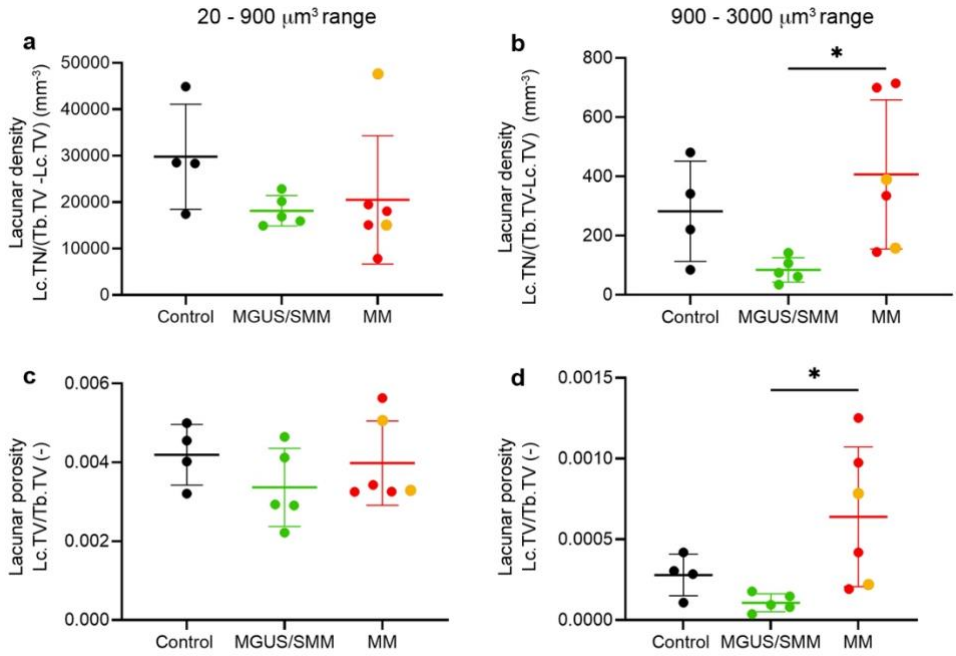

Figure 5. Lacunar density and microporosity analysis for the small lacunae 20-900 µm³ range and for the larger lacunae 900-3000 µm³ range. Lacunar density calculated as the total number of osteocyte lacunae (Lc.TN) normalized to the trabecular bone volume and excluding lacunar total volume (Tb.TV-Lc.TV), for each group control, MGUS/SMM and newly diagnosed MM (samples with bone lytic lesion in red, samples without lytic lesions in orange). Microporosity calculated as lacunar total volume (Lc.TV) divided by trabecular total bone volume (Tb.TV) for each group. Error bars indicate mean ± SD. One way ANOVA with Tukey's multiple comparison test *$p<0.05$.

Figure 6

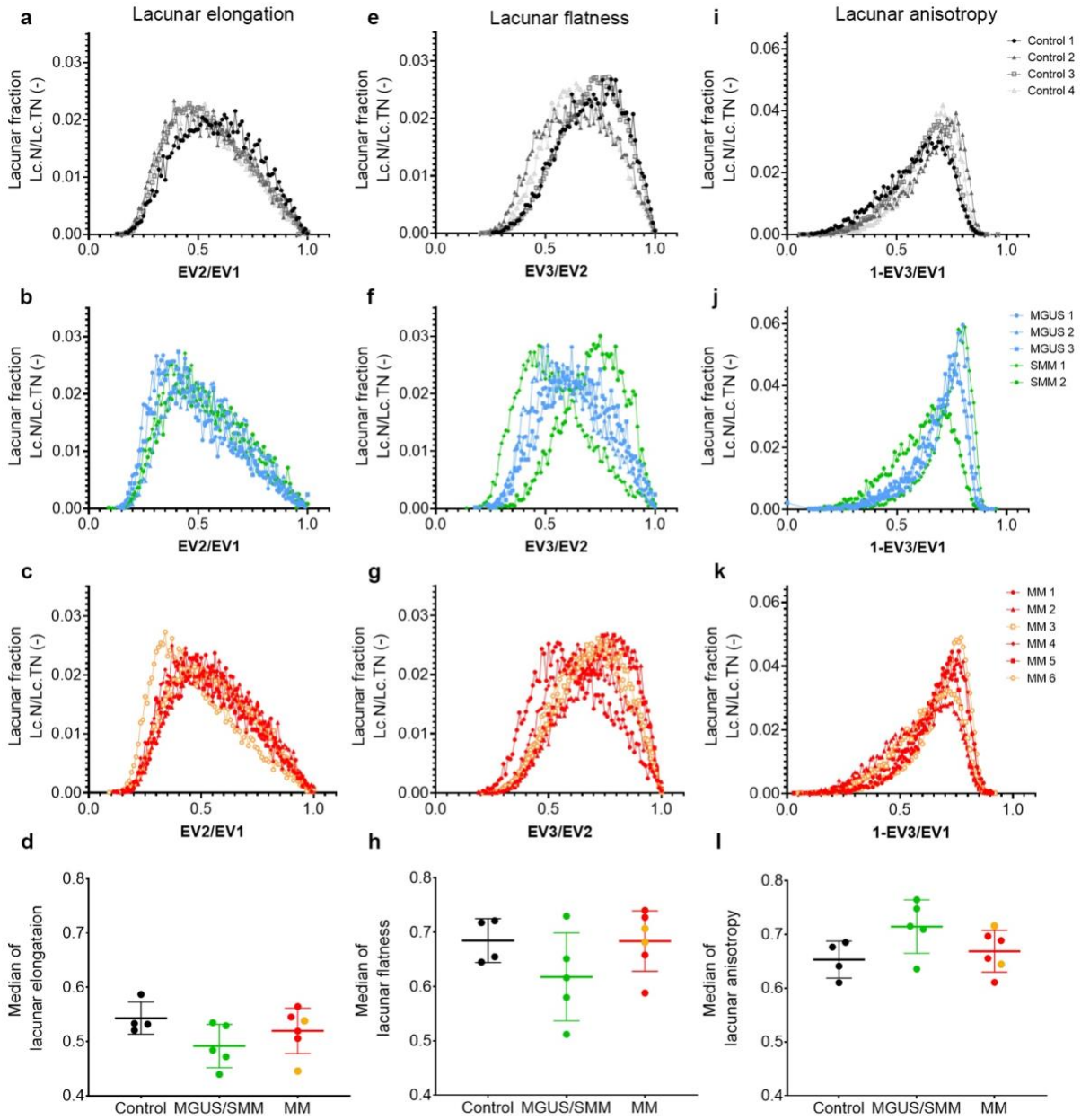

Figure 6. Lacunar morphological analysis for the small lacunae 20-900 µm³ range. Lacunae elongation, flatness and anisotropy analysis for (a, e, i) control, (b, f, j) MGUS/SMM and (c, g, k) MM groups. Individual lacunae were assigned with eigenvalues (EV1, EV2 and EV3) to then calculate lacuna elongation as EV2/EV1 (with lower values for elongated and 1 for spherical) as (a-c) lacunar fraction (Lc.N/Lc.TN) and as (d) median of all lacuna elongation values for each sample; lacuna flatness as EV3/EV2 (ranging from 0 for flat to 1 for spherical) as (e-g) lacunar fraction (Lc.N/Lc.TN) and as (h) median of all lacuna flatness values for each sample; and lacuna anisotropy as 1-EV3/EV1 (with smaller values for isotropic/spherical and 1 for highest anisotropy) as (i-k) lacunar fraction (Lc.N/Lc.TN)

and as (l) median of all lacuna anisotropy values for each sample. Sample from the Jamshid biopsy in black, all other control samples in grey. MGUS in blue, SMM in green, MM samples with bone lytic lesion in red, MM samples without lytic lesions in orange. Error bars indicate mean ± SD.

Tables

Table 1. Clinical data from MGUS patients from the University Hospital Würzburg

Parameters			
biopsy number	MGUS 1	MGUS 2	MGUS 3
age (years)	71	60	68
gender	f	m	f
immunoglobulin subtype	IgG lambda	IgG kappa	IgG kappa
r-ISS	not applicable	not applicable	not applicable
cytogenetic risk	not applicable	not applicable	not applicable
M-protein [g/L]	not detectable	not detectable	1,2
heavy chain [mg/dL, normal range]	1382 (610-1616)*	881 (610-1616)	507 (610-1616)
involved serum free light chain (sFLC) [mg/L, normal range]	23,89 (5,71-26,30)	10,75 (3,30-19,40)	215 (3,30-19,40)
ratio (involved / uninvolved sFLC)	0,86	1,02	5,44
bone marrow infiltration of $CD138^+$ cells [%]	<10	<10	<5
CT findings of osteolytic lesion	none	none	none
hemoglobin [g/dL]	12,9 (12-16)	14,4 (13,5-16,9)	12,7 (12-16)
creatinine [mg/dL]	0,63 (0-0,95)	1,06 (0-1,17)	6,69 (0-0,95)
cytogenetics**	no aberration	no aberration	no aberration
calcium [mmol/L]	2,2 (2,0-2,7)	2,5 (2,0-2,7)	2,3 (2,0-2,7)
alkaline phosphatase [U/L]	51 (35-105)	72 (35-105)	not available
inorganic phosphate [mmol/L]	1,09 (0,87-1,45)	1 (0,87-1,45)	1,85 (0,87-1,45)
bone anti-resorption treatment (duration)	Denosumab (four months)	no	no

* Values in brackets show the normal range for the parameters, respectively

** Cytogenetic alterations by fluorescence in situ hybridization (FISH)

Table 2. Clinical data from SMM patients from the University Hospital Würzburg

Parameters		
biopsy number	SMM 1	SMM 2
age (years)	46	70
gender	f	m
immunoglobulin subtype	IgA kappa	IgA lambda
r-ISS	II	I
cytogenetic risk	high risk	standard risk
M-protein [g/L]	not detectable	13,42
heavy chain [mg/dL, normal range]	1826 (88-410)	2826 (88-410)
involved serum free light chain (sFLC) [mg/L, normal range]	11,82 (3,30-19,40)	54,99 (5,71-26,3)
ratio (involved / uninvolved sFLC)	1,33	12,03
bone marrow infiltration of $CD138^+$ cells [%]	10-15	20-30
CT findings of osteolytic lesion	none	none
hemoglobin [g/dL]	12 (12-16)	13,2 (13,5-16,9)
creatinine [mg/dL]	0,78 (0-0,95)	0,91 (0-1,17)
cytogenetics	t4;14, gain of 1q21	del13q14
calcium [mmol/L]	2,2 (2,0-2,7)	2,4 (2,0-2,7)
alkaline phosphatase [U/L]	59 (35-105)	40 (35-105)
inorganic phosphate [mmol/L]	1,08 (0,87-1,45)	1,23 (0,87-1,45)
bone anti-resorption treatment (duration)	not known	no

Table 3. Clinical data from newly diagnosed MM patients from the University Hospital Würzburg

Parameters			
biopsy number	MM 1	MM 2	MM 3
age (years)	58	57	72
gender	m	m	f
immunoglobulin subtype	IgG kappa	kappa	IgG lambda
r-ISS	III	II	III
cytogenetic risk	high risk	standard risk	high risk
M-protein [g/L]	35,3	not detectable	20,6
heavy chain [mg/dL, normal range]	4765 (610-1616)	not available	3074 (610-1616)
involved serum free light chain (sFLC) [mg/L, normal range]	71,12 (3,30-19,40)	8260 (3,30-19,40)	1376 (5,71-26,3)
ratio (involved / uninvolved sFLC)	40,41	890,09	355,56
bone marrow infiltration of $CD138^+$ cells [%]	70	60-70	90
CT findings of osteolytic lesion	osteolytic lesion with extraosseous soft tissue mass in spine (T12), lytic lesion in pelvis, rib series fractures, medullary lesions in femora and humeri, reduced bone mineral density	disseminated osteolysis in spine, one large lesion in T9 with increased fracture risk, old vertebral body collapse in T7 and fracture of the fourth left rib, multiple small osteolyses in scapulae, ribs, sternum reduced bone mineral density	no osteolytic lesions medullary lesions in upper and lower limbs, spine, sternum; reduced bone mineral density
hemoglobin [g/dL]	10,8 (13,5-16,9)	10,7 (13,5-16,9)	10,2 (12-16)
creatinine [mg/dL]	0,83 (0-1,17)	2,3 (0-1,17)	0,72 (0-0,95)
cytogenetics	t14;16, gain of 1q21	t11;14	del 17p, 1q gain, del14q, del 4p, del 16q, del 5p
calcium [mmol/L]	2,3 (2,0-2,7)	2,9 (2,0-2,7)	2,5 (2,0-2,7)
alkaline phosphatase [U/L]	97 (35-105)	80 (35-105)	49 (35-105)
inorganic phosphate [mmol/L]	1,25 (0,87-1,45)	1,33 (0,87-1,45)	0,99 (0,87-1,45)

bone anti-resorption treatment (duration)	bisphosphonate (zoledronic acid) for one month	no	no

Table 3 (cont). Clinical data from newly diagnosed MM patients from the University Hospital Würzburg

Parameters			
biopsy number	MM 4	MM 5	MM 6
age (years)	60	68	64
gender	m	f	f
immunoglobulin subtype	IgA lambda	IgG kappa	IgG kappa
r-ISS	II	II	II
cytogenetic risk	standard risk	standard risk	standard risk
M-protein [g/L]	32,6	4,5	7,4
heavy chain (mg/dL, normal range)	4000 (88-410)	1180 (610-1616)	1625 (610-1616)
involved serum free light chain (sFLC) [mg/L, normal range]	33,8 (5,71-26,3)	16,59 (3,30-19,40)	309,8 (3,30-19,40)
ratio (involved / uninvolved sFLC)	4,26	1,49	8,41
bone marrow infiltration of $CD138^+$ cells [%]	30	50	60
CT findings of osteolytic lesion	osteolytic lesion in pelvis; mild reduction in bone mineral density	disseminated osteolysis in skull, spine, fracture series in spine (T7, 8, 11; L1, 2, 4), reduced bone mineral density in spine	none
hemoglobin [g/dL]	14 (13,5-16,9)	10,1 (12-16)	12,8 (12-16)
creatinine [mg/dL]	0,96 (0-1,17)	1,02 (0-0,95)	0,91 (0-0,95)
cytogenetics	del 1p32, del13q14, gain of 1q21	trisomy 11	gain of 1q21
calcium [mmol/L]	2,4 (2,0-2,7)	2,5 (2,0-2,7)	2,4 (2,0-2,7)
alkaline phosphatase [U/L]	41 (35-105)	95 (35-105)	92 (35-105)
inorganic phosphate [mmol/L]	1,19 (0,87-1,45)	0,94 (0,87-1,45)	0,74 (0,87-1,45)
bone anti-resorption treatment (duration)	no	no	no

Table 4. Control samples: Jamshidi bone biopsy from a patient at the University Hospital Würzburg and samples from autopsies at the Ludwig Boltzmann-Institute of Osteology, Vienna.

Parameters				
biopsy number	control 1	control 2	control 3	control 4
type of biopsy	jamshidi	autopsy*	autopsy*	autopsy*
age (years)	69	64	57	63
gender	f	f	f	f
previous disease	myelodysplastic syndrome	not known	not known	not known

* Subset of an earlier cohort presented previously [8] and re-evaluated here

Table 5. Nomenclature for osteocyte lacunar volume analysis

Nomenclature	**Abbreviation**	**Unit**
Number of osteocyte lacunae	Lc. N	-
Total number osteocyte lacunae	Lc. TN	-
Lacunar volume	Lc. V	µm³
Total lacunar volume	Lc. TV	µm³
Trabecular bone volume	Tb. BV	µm³

Table 6: Nomenclature for osteocyte lacunar morphological analysis

Parameter	**Definition**	**Unit**	**Formula**
Normalized lacunar volume frequency distribution	Number of lacunae volume divided by the trabecular bone total volume minus the lacuna total volume	#/µm³	$\frac{\Sigma\, Lc.N}{Tb.TV\ -\ Lc.TV}$
Lacunar volume cumulative distribution	Sorted sum of volume divided by total volume	-	
Microporosity	Total lacunar volume with respect to the total trabecular bone volume	-	$\frac{Lc.TV}{Tb.TV}$
Lacuna elongation	0 for elongated 1 for spherical	-	$\frac{EV2}{EV1}$
Lacuna flatness	0 for flat 1 for spherical	-	$\frac{EV3}{EV2}$
Lacuna anisotropy	0 for isotropic, spherical 1 for highly anisotropic	-	$1 - \frac{EV3}{EV1}$

768